Journal of Applied Sciences

ISSN 1812-5654

science alert

ANSInet
an open access publisher
http://ansinet.com

Journal of Applied Sciences 12 (6): 518-534, 2012
ISSN 1812-5654 / DOI: 10.3923/jas.2012.518.534

Assessment of Contrast Positioning Effects on Reconstructed Images of Elliptical Models in EIT Applying Different Current Patterns

[1]Ashkan Javaherian, [2]Amir Movafeghi, [1]Reza Faghihi and [3]Effat Yahaghi
[1]Department of Mechanical Engineering, Shiraz University, Iran
[2]Reactors and Accelerators Research and Development School,
Nuclear Science and Technology Research Institute, Tehran, Iran
[3]Department of Physics, Imam Khomeini International University of Qazvin, Iran

Abstract: This study investigates the effects of contrast region positioning on reconstructed EIT images, using an elliptical model in which a contrast displaces aligned by the horizontal and vertical axes of the ellipse. Different common current-voltage patterns have been applied as well. The results obtained from the elliptical model could be applicable for estimating the anisotropy or ellipticity effects of the human body's cross-section on reconstructed EIT images. The models are defined based on two variable factors which are either the direction of the contrast movement in the ellipse, or different current-voltage patterns. The ability of the various current-voltages patterns to reconstruct images of the moving contrast as a function of contrast positioning in the models is compared. This ability has been investigated using four figures of merit which are the distinguishability of the forward models and also blur radius, artefact amplitude measure and position error of the reconstructed images. This comparison can be useful in cases in which the Region of Interest (ROI) location has been estimated before EIT measurements via either anatomical structure mapping or using other modalities such as ultrasound, MRI, etc. In addition, we show that the distinguishability measures cannot definitively be an exhaustive criterion for predicting the quality of the reconstructed images.

Key words: Electrical impedance tomography, contrast positioning, current patterns, elliptical models

INTRODUCTION

Electrical impedance measurements have many applications in the engineering and science (Kumar *et al*., 2006; Lohcham *et al*., 2002; Ghorbel *et al*., 2006). Among them, biomedical devices use the bio-impedance measurements in many fields such as blood flow and body composition (Hassan *et al*., 2008; Elwakkad *et al*., 2011; Mirhosseini *et al*., 2011).

Electrical Impedance Tomography (EIT) is a diffuse imaging technique which maps the interior distribution of the electrical properties within a medium (Saulnier *et al*., 2001). In this modality, a series of electrodes (usually 16 to 64) are attached to the medium's periphery. Low amplitude alternating electrical currents (0.1-1.0 mA) in a frequency range from approximately 10 kHz to about 1 MHz are injected through a set or all of the electrodes and the corresponding voltages are measured on a limited number of chosen or all electrodes (Noor, 2007). The objective is to estimate cross-sectional conductivity or permittivity distribution based on these voltage measurements. This can be implemented by numerical inversion of a linearized form of equations relating measured voltages to injected currents. This boundary current-voltage data set has been called the Neumann-to-Dirichlet (NtD) map (Jing-Lei and Zhi-Jian, 2011). This is an inverse problem which is usually solved based on Finite Element Methods (Binjadhnan and Ahmad, 2010; Keto *et al*., 2006). EIT reconstruction is quite badly posed due to the insensitivity and nonlinearity between the NtD map and the internal conductivity distribution. Hence, an augmented regularization term must be included in object function in order to obtain a stable solution (Vauhkonen *et al*., 1998).

Electrode position uncertainties and electrode displacements that occur during voltage measurements are two key error sources in EIT (Soleimani *et al*., 2006). In clinical applications, the shape of the boundary, a part of human body on which the measurement electrodes are

Corresponding Author: Amir Movafeghi, Scientific Staff Member, Nuclear Science and Technology Research Institute, Tehran, Iran Tel: (+98) 2182061 Fax: (+98) 2188221226

attached, may be changed. For example, in thoracic imaging, electrode displacements occur due to respiration or posture changes. These errors lead to an increase in the artifacts in the reconstructed images (Adler *et al*., 2009; Zhang and Patterson, 2005). These problems arise since EIT measurements are imposed onto a model that approximates the geometry of a medium's boundary and therefore, the uncertainty of positioning or the displacement of electrodes reduce the reliability of the reconstruction model. However, there are important assumptions that are made with respect to EIT algorithms. These methods usually assume the object to be a 2D circular disk and the electrodes to be placed equidistantly along the circular boundary. In reality, these assumptions are far from being true, especially in medical applications. Thus, these are the main sources of image distortion in EIT, as it can be one of the major causes of errors in the measured voltages. The NtD map is strongly affected by electrode position uncertainties and boundary geometry of the object being imaged. Even very small errors can cause large artifacts in images due to ill-posedness of the problem. Here, the importance of investigating these kinds of errors can be seen.

Previously, several groups tried to assess and compensate the effects of boundary shape variations (Abbasi *et al*., 2009; Loke and Dahlin, 2002; Kolehmainen *et al*., 2006). The best alternative is an algorithm which reconstructs both the conductivity change image and the electrode displacement from difference measurement data, which is called proposed algorithm in this study. The inverse problem has been solved in terms of one step "Maximum A Posteriori" regularized inverse, in which an augmented Jacobian is constructed via perturbation in both conductivity changes and electrode displacements (Soleimani *et al*., 2006).

This study has implemented this algorithm in order to reconstruct both conductivity changes and electrode displacements in a 2D elliptical model, instead of the simple circular models used in previous similar works. The geometry of domains is anisotropic in clinical applications such as muscle tissue or flowing blood. So the results obtained from the elliptical models can be useful for estimating the anisotropy and ellipticity effects of the human body's cross-section on reconstructed images.

The effects of contrast region positioning on the reconstructed images using the elliptical model with an inhomogeneity which moves aligning the horizontal and vertical axes of the model are also investigated. The proposed models in this study are defined based on two factors. The first factor is the direction of inhomogeneity moving in the models, and the second is the pattern that has been applied for stimulating current and measuring corresponding voltage. In this study, four current-voltage pattern protocols, neighboring, opposite, cross and trigonometric patterns are applied (Vauhkonen, 1997). We comment that designing EIT systems which have ability to apply different current-voltage patterns can be useful for clinical EIT experimenters to select optimum current-voltage patterns based on the region of interest considered in a human body's organ. In clinical situations, the contrast positioning can be determined using anatomical structure mapping or other imaging modalities. Furthermore, in this study, the errors due to electrode displacements in the elliptical reconstruction model are investigated by using a standard algorithm, compensated by applying the proposed algorithm and finally, the obtained results are compared. By assessing these results, we estimate not only the sensitivity of artifacts in the reconstructed images to electrode displacements, but also the ability of the proposed algorithm for reducing these errors when various current-voltage patterns are applied.

The reconstruction models used in this study consist of:

- An elliptical model with a 16-electrode measurement system in which the neighboring current-voltage pattern has been applied. The contrast moves from the left to the right side of the ellipse aligned by the major axis and 9 frames of movement are considered
- An elliptical model with a 16-electrode measurement system in which the neighboring current-voltage pattern has been applied. The contrast moves from the bottom to the top side of the ellipse aligned by the minor axis and 5 frames of movement are considered
- An elliptical model with a 16-electrode measurement system in which the current stimulation and voltage measurement are respectively based on the opposite and adjacent patterns. The contrast moves from the left to the right side of the ellipse aligned by the major axis and 9 frames of movement are considered
- An elliptical model with a 16-electrode measurement system in which the current stimulation and voltage measurement are respectively based on the opposite and adjacent patterns. The contrast moves from the bottom to the top side of the ellipse aligned by the minor axis and 5 frames of movement are considered
- An elliptical model with a 16-electrode measurement system in which the cross current-voltage pattern has been applied. The contrast moves from the left to the right side of the ellipse aligned by the major axis and 9 frames of movement are considered

- An elliptical model with a 16-electrode measurement system in which the cross current-voltage pattern has been applied. The Contrast moves from the bottom to the top side of the ellipse aligned by the minor axis and 5 frames of movement are considered
- An elliptical model with a 16-electrode measurement system in which the trigonometric current-voltage pattern has been applied. The contrast moves from the left to the right side of the ellipse aligned by the major axis and 9 frames of movement are considered
- An elliptical model with a 16-electrode measurement system in which the trigonometric current-voltage pattern has been applied. The contrast moves from the bottom to the top side of the ellipse aligned by the minor axis and 5 frames of movement are considered

For each model, first, the distinguishability values of forward model have been calculated as a function of contrast positioning and then, conductivity change images have been reconstructed for all frames in the three cases that are introduced as follows:

- The model's boundary has been assumed to have no deformation. So the electrodes have no displacement and the images have been reconstructed using the standard algorithm
- The model's boundary has been assumed to have deformation with a magnitude in the order of 1% radial position of the surface nodes when the centre of the ellipse is placed on the origin of the coordinate system. The images have been reconstructed using the standard algorithm in order to assess the deformation effects on the reconstructed images
- The boundary deformation has been assumed the same as case 2, but the images have been reconstructed using the proposed algorithm in order to reduce errors due to electrode displacements

MATERIALS AND METHODS

In this study, the EIDORS-V3.4 (Electrical Impedance and Diffuse Optical Reconstruction Software) suite has been used in MATLAB environment (Polydorides and McCann, 2002; Adler and Lionheart, 2006).

Forward solution: In the standard algorithm, the length of unknown parameter vector x is equal to the number of elements in the FEM model $x = \sigma$, whereas in the proposed algorithm, the length of vector x is equal to the number of FEM elements plus the number of electrode movement parameters DL, where D is the dimension of the reconstruction model (2D or 3D) and L is the number of electrodes around the object being imaged. Therefore, vector x can be written as:

$$x = \begin{bmatrix} \sigma \\ r \end{bmatrix} \quad (1)$$

where, r is a vector that includes electrode displacements in 2 or 3 dimensions and has the length of DL and σ is a vector whose elements are the FEM elements' conductivity change and has the length of N.

Applying the standard algorithm, the forward solution is the computation of difference measurement data δV from conductivity changes $\delta x = \delta\sigma$. The Jacobian matrix is formed based on perturbation method in order to linearize the forward problem. Each member $[j]^{ij}$ is calculated by integrating over element Δn for independent measurement I = (l,k) from the lth electrode and kth current pattern as follows (Polydorides and Lionheart, 2002):

$$\frac{\partial V_l^k}{\partial x_n} = \int_{\Delta n} \nabla v_k . \nabla v_l dv \quad (2)$$

where, v_k represents the voltage distributions computed when the kth current pattern is used, v_l represents the electric potential calculated in terms of voltage measurement on the lth electrode and V_i^k is voltage measured on the lth electrode when the kth current pattern is applied.

In the proposed algorithm, the forward solution is the computation of difference measurement data δv from both the conductivity change image $\delta\sigma$ and the electrode movements $\delta\vec{r}$. Therefore, the inverse problem is formulated and regularized using an augmented Jacobian constructed via perturbation in both the conductivity of each element and the position of each electrode (Soleimani *et al*., 2006). The electrode displacement Jacobian J_r is a submatrix which is added to standard conductivity Jacobian $J\sigma$. So, the new Jacobian matrix is formed as:

$$J = [J_\sigma, J_r] \quad (3)$$

By this definition, each element of the augmented Jacobian J_r is the sensitivity of each element of measurement data boundary V to the displacement of each electrode with position vector $r \in R^2$ for 2D models. Therefore, the electrode displacement Jacobian matrix is constructed as:

$$J_m = \begin{bmatrix} \frac{\delta V}{\delta r_1} \cdots \frac{\delta V}{\delta r_{2L}} \end{bmatrix} \quad (4)$$

Inverse solution: Generally, the methods used for solving inverse problems are categorized as deterministic and probabilistic methods. In deterministic methods, unknown vector x is non-random, whereas in statistical methods, its elements are random variables (Vauhkonen, 1997). The methods usually used for solving ill-posed inverse problems statistically are based on regularized "Maximum A Posteriori" frame work and are discussed below (Adler and Lionheart, 2011).

Assume the following model for boundary measurement:

$$\begin{matrix} V = v + n \\ v = F(x) \end{matrix}, \; F: R^{N+DL} \to R^{LK} \tag{5}$$

where, F represents forward operator, N+DL is the length of vector x and LK is the number of independent measurements. Measured voltages on electrodes and noise in data measurements (V, n) are random parameters.

Given x, the measurement vector V and noise vector n have the same density except that mean differs:

$$E(V) = F(x) + E(n) \tag{6}$$

Therefore, the density p (V) given x will be:

$$p(V|x) = p_n(V - F(x)|x) \tag{7}$$

Assuming that x and n are independent vectors and vector n is Gaussian with zero mean, the conditional density of measurement data will be in the form as:

$$p(V\left|x\right.) \propto \exp\left\{-\frac{1}{2}(V - F(x))^T c_n^{-1}(V - F(x))\right\} \tag{8}$$

where, c_n is measurement noise correlation matrix. The noise is assumed as Additive White Gaussian Noise (AWGN) and thus, c_n is constructed as a diagonal matrix of the noise variance associated with each electrode. Assuming that the variance of measurement noise for all the electrodes is equal, c_n will be constructed as:

$$[c_n]_{ii} = \frac{var(n)}{(V_i)^2} \tag{9}$$

where, var (n) is the variance of measurement noise and V_i is the ith measured voltage. $p(V|x)$ is called likelihood function. For given data V, $\hat{x}_{ML} = \hat{x}_{ML}(x)$ is the Maximum Likelihood estimate (ML), if V is maximized. The maximization of $p(V|x)$ is identical to the minimization of:

$$\phi_{ML}(x) = \frac{1}{2}(V - F(x))^T c_n^{-1}(V - F(x)) \tag{10}$$

The ML estimate is useful for solving well-posed problems. These problems do not need to be regularized. However, the inverse problem in EIT is badly posed and therefore the problem has to be modified in order to obtain a stable solution. The idea of the regularization method is to replace the ill-posed problem by a nearby well-posed problem. In the probabilistic approach, MAP estimation is used if regularization is required. According to Bayes theorem, the posterior density can be written as:

$$\begin{aligned} p(x\left|V\right.) &\propto \exp\left\{-\frac{1}{2}(V - F(x))^T c_n^{-1}(V - F(x))\right\} p(\sigma) \\ &\propto \exp\left\{-\tfrac{1}{2}(V - F(x))^T c_n^{-1}(V - F(x)\right\} \\ &\bullet \exp\left\{-\frac{1}{2}(x - x_0)^T c_x^{-1}(x - x_0)\right\} \end{aligned} \tag{11}$$

where, x_0 is assumed to be the expected changes in the unknown parameters. Without any specific knowledge about the medium being measured, conductivity changes are assumed to be equally zero and the expected image is therefore one of no conductivity change and is modeled by $x_0 = 0$.

C_x is the covariance matrix of the unknown parameter vector. In the standard algorithm, this matrix includes information on the amplitude of the image and also spatial frequency distribution. The diagonal elements $[c_x]_{ij}$ represent the variance of amplitude of each FEM element, whereas the off diagonal element (i,j) is a function of the correlation coefficient η between the ith element and the jth element. The image covariance matrix can be written as:

$$[c_x]_{ij} = \eta\sqrt{[c_x]_{ii}[c_x]_{jj}} \tag{12}$$

Because of the low spatial resolution in EIT, the spatial frequency of the reconstructed conductivity image has little high frequency content. Thus, the adjacent FEM elements will have correlated reconstructed values. For instance, using 16 electrodes, there is not enough information on the order of 5% of the medium diameter. Therefore, it can be assumed that elements closer than this distance are highly correlated and elements further apart are not correlated. According, to this point, the matrix c_x can be interpreted as a spatial low pass filter. Furthermore, this matrix is numerically unstable and difficult to invert. Therefore, a regularization matrix c^{-1}_x is directly constructed using a high pass filter. In this study,

a Gaussian high pass filter in the form of the equation below in the frequency domain is considered (Adler *et al*., 2009):

$$G(u,v) = 1 - e^{-w_0(u^2+v^2)} \quad (13)$$

where, w_0 is the cut-off frequency of the high pass filter. After transforming to continuous spatial domain, the equation can be rewritten in the form as:

$$G(x,y) = \delta(x,y) - \frac{\pi}{w_0^2} e^{-(\frac{\pi^2}{w_0^2})(x^2+y^2)} \quad (14)$$

where, δ (x, y) is Dirac delta function. This formulation must be transformed to the discrete spatial domain due to the FEM nature of the reconstruction models in EIT.

$$G_{ij} = \int_{E_j} [\delta(x - x_i, y - y_i) - \frac{\pi}{w_0^2} e^{-\frac{\pi^2}{w_0^2}((x-x_i)^2+(y-y_i)^2)}] dxdy \quad (15)$$

where, G is the filtering matrix which multiplies the image vector x = σ to give a filtered image G_x. This matrix is constructed by centring the high pass filter in the ith element and integrating across the jth element, where (x_i, y_j) is the centre of the ith element and E_j is the area of the jth element (Adler and Lionheart, 2006). The regularization matrix is finally formed as:

$$c_x^{-1} = \sigma_x^2 G^T G \quad (16)$$

This matrix includes some filtering in all spatial frequencies. Therefore regularization improves the ill-posedness of the inverse solution, but degrades the spatial resolution.

Applying the proposed algorithm, c_x^{-1} has been separated into two parts that represent the conductivity changes of the elements and electrode displacements (Soleimani *et al*., 2006; Griffiths, 2001):

$$c_x^{-1} = C = \begin{bmatrix} C_\sigma & 0 \\ 0 & C_r \end{bmatrix} \quad (17)$$

where, C_σ of size N×N is the inter-element conductivity change inverse covariance and C_r of size L×L is the inter-electrode movement inverse covariance. The conductivity and electrode movement components are assumed to be uncorrelated. Therefore, the cross-covariance of these vectors is zero. C_σ is modelled using Laplacian high pass filter in order to model the expected smoothness of the actual conductivity change images. The electrode movement part C_r should also include some kind of inter-electrode correlation, since, as the boundary deforms smoothly, the adjacent electrodes may be misplaced similarly. The inter-electrode displacement correlation is modelled using a discrete Laplacian filter, with the diagonal elements $[C_r]^{ij}$ = 2.1p (Soleimani *et al*., 2006). Notice that:

$$p = \frac{w_\sigma^2}{w_r^2}$$

is defined as the electrode displacement parameter to represent the compromise between the model fidelity to the conductivity change image and the electrode movement, where w_σ^2 and w_σ^2 are a priori assumptions of amplitudes of conductivity change and electrode displacement, respectively. Since, the conductivity change is assumed on the order of homogeneity conductivity and electrode displacement is assumed on the order of 1% of the medium diameter, p is selected to be 100. The off-diagonal elements $[C_r]^{ij}$ are set to be -p for the adjacent electrodes (Soleimani *et al*., 2006). The maximum a posteriori estimate is obtained by maximizing the posterior density which is identical to the minimization of:

$$MAP(x) = \frac{1}{2}(V - F(x))^T c_n^{-1}(V - F(x)) + \frac{1}{2}(x - x_0)^T c_x^{-1}(x - x_0) \quad (18)$$

where, MAP (x) is object function. F (x) is replaced by J (x) in order to linearize the forward problem:

$$\hat{x}_{MAP} = (J^T c_n^{-1} J + c_x^{-1})^{-1}(J^T c_n^{-1} V + c_x^{-1} x_0) \quad (19)$$

As priori amplitudes of conductivity change, electrode displacement and noise are measured in different units, so they may be of different orders of magnitude (Soleimani *et al*., 2006). Therefore, the inverse covariances in Eq. 11 must be rewritten in a weighted matrix form as:

$$\begin{aligned} c_x^{-1} &= \frac{1}{w_\sigma^2} C'_\sigma + \frac{1}{w_r^2} C'_r,\ c_n^{-1} = \frac{1}{w_n^2} C'_n \\ C_r &= \frac{1}{w_r^2} C'_r,\ C_\sigma = \frac{1}{w_\sigma^2} C'_\sigma \end{aligned} \quad (20)$$

where, w_n^2 is a priori amplitude assumption for noise measurements similar to conductivity changes and electrode displacements. Plugging Eq. 20 into Eq. 19 and considering that x_0= 0, the MAP estimation for difference algorithm will be:

$$\delta\hat{x}_{MAP} = (J^T \frac{1}{w_n^2} C'_n J + \frac{1}{w_\sigma^2} C'_\sigma + \frac{1}{w_r^2} C'_r)^{-1}(J^T \frac{1}{w_n^2} C'_n \delta V) \quad (21)$$

The Eq. 21 can be considered as a function of hyperparameter λ and electrode movement parameter p. Therefore, the estimation is rewritten as:

$$\delta\hat{x}_{MAP} = (J^T J + \lambda(C'_o + pC'_r))^{-1} J^T \delta V \quad (22)$$

Consider that C'_n is assumed to be an identity matrix and λ is hyperparameter, which is in the form of:

$$\lambda = \frac{w_n^2}{w_o^2} \quad (23)$$

For each of the models, the optimal values for the hyperparameter are calculated via minimizing the blur radius in the images reconstructed by applying a specified range of hyperparameters (Graham and Adler, 2006).

RESULTS

Forward models: The forward model is implemented as an elliptical FEM model with an axis ratio of 2, so that semi major axis is aligned by horizontal axis and has a length of 1 and the centre is located on the origin of the coordinate system. The forward model is made up of 1185 nodes and 2240 triangular elements.

Point electrode model is considered, in which 16 nodes on the boundary with equal distance to each other are selected to represent electrodes. Current-voltage patterns used for injecting current and measuring corresponding voltages on electrodes are neighboring, opposite, cross and trigonometric patterns. In medical applications, the total input current constraint is important since the medical safety regulations limit the total input current that can be applied to human body. The maximum amplitude of the total injected current in each synchronous stimulation is set to be 10 mA as the maximum patient auxiliary current specified by (IEC, 2005). For bipolar stimulation, this represents 10 mA flowing from one stimulating electrode to another per electrode, whereas for trigonometric pattern, the total current through all applied parts is assumed to be $||I||_l$ = 10 mA. In addition, a 20 dB Additive White Gaussian Noise (AWGN) is simulated in the measurement data.

The homogenous region has the conductivity of 1 s m^{-1}. Certain elements are selected to represent an inhomogeneity like a disk with a radius of 0.1 and conductivity of twice the other elements. The contrast moves aligning the horizontal and vertical axes of the ellipse from the left to right or the bottom to top side of the models and some frames of these movements are reconstructed. These frames are chosen so that the inhomogeneity centre is translated between the frames equidistantly and the distance of each translation would be 0.2.

Distinguishability measure: Distinguishability is a measure of the ability of an EIT system to detect small conductivity changes (Adler *et al*., 2011). It can be considered as the most applicable primary measure of the performance of an EIT system for solving forward problem. Distinguishability values depend on factors such as the current stimulation amplitude, the accuracy of voltage measurement, the number and placement of electrodes or the selected current-voltage patterns. In this study, it is shown that distinguishability values change not only for different points across the entire medium, but also for each point by applying different current patterns. Fig. 1a and b show, respectively the variations of distinguishability values for the various points aligning the horizontal and vertical axes of the ellipse, using different current patterns. These values have been calculated from the refined FEM of the elliptical model with 72193 nodes and 143360 elements. A small inhomogeneity has been introduced with a radius of 0.02 and conductivity of 2 s m^{-1}, which moves aligning

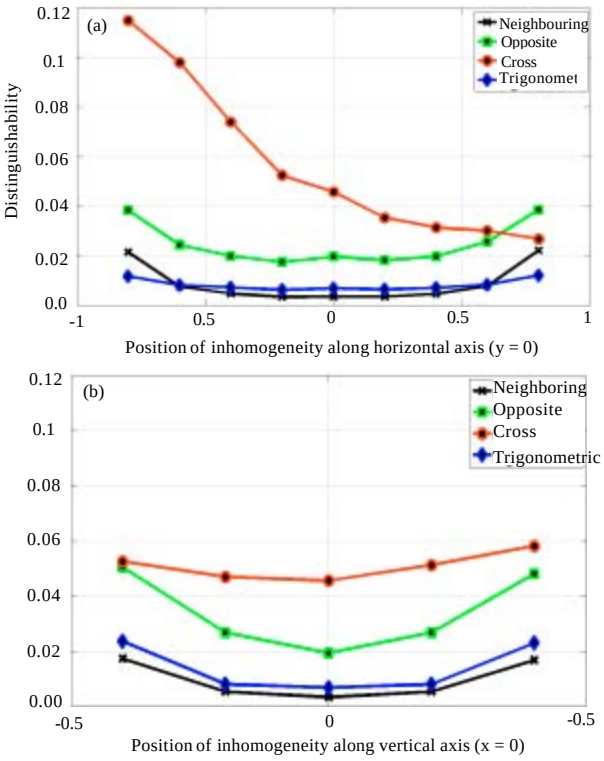

Fig. 1: The distinguishability variations versus contrast positioning for the models along, (a) The major axis and (b) The minor axis

the mentioned axes of the ellipse. Since, we only attempt to solve the forward problem for calculating this measure, applying a much finer FEM model does not lead to any problem.

According to Fig. 1a, for the models in which the neighboring, opposite or trigonometric current patterns have been applied, the distinguishability decreases symmetrically when the considered point moves aligning the major axis from the boundary to the centre of the ellipse. This is due to not only the attenuation of current density, but also divergence of the current flow and isopotential lines from the boundary to the centre of the ellipse. Consider that the symmetry of current stimulation and voltage measurement with respect to the minor axis major axis in both sides of the minor axis for these patterns. From Fig. 1a, comparing these three current patterns, the highest gradient of decrease is observable for the neighboring current pattern while the smoothest has occurred for the trigonometric pattern.

However, the cross current pattern leads to different results. The distinguishability increases sharply when the considered point translates aligned by the horizontal axis from the right to the left side of the ellipse. This is because, applying this pattern, the current and voltage reference electrodes are set in the auxiliary positions, so that these reference electrodes do not rotate around the entire periphery of the ellipse. In other words, applying cross pattern, two sequences of measurements are obtained with respect to two adjacent reference voltage electrodes. These reference electrodes are located in the middle of two other electrodes used as the current reference electrode in the two sequences.

Such pattern has led to a much higher current density and so, greater distinguishability values in the regions closer to the reference electrodes. In this study, the current reference electrodes are electrode 16 and 3, considering that electrode 1 is located on (-1, 0) and the other electrodes are positioned clockwise. So, the increase in distinguishability for the points which are closer to the reference electrodes is predictable. In addition, the cross current pattern has led to much higher distinguishability values in the entire medium, while the opposite, trigonometric and neighboring patterns have been located in the next rankings, respectively. The results obtained from Fig. 1b are approximately similar to Fig. 1a except that the asymmetry of the values resulting from the model with the cross pattern has been modified because of the symmetrical positioning of the mentioned current reference electrodes with respect to horizontal axis. However, as reference electrode 3 (upper reference electrode) has a greater distance to the horizontal axis than electrode 16, the values for the points which are upside the horizontal axis has become slightly greater than those of the downside ones.

These results are not far from the previous ones obtained from former studies for circular isotropic homogenous models. These studies reported better results for the opposite and trigonometric current patterns than the neighboring one, especially in the centre of the circular models (Oh and Sadleir, 2005; Adler *et al*., 2011). This was due to the uniformity of current density distributions across the entire medium that leads to a much higher sensitivity in the circular models, especially in central region, when the trigonometric or opposite current pattern has been applied. In this study, the cross pattern has led to much higher distinguishability than all the other patterns in the entire medium. This agrees with the results obtained from the previous works in this term (Holder, 2004). However, those studies are focused on parameters such as current density distribution or distinguishability and do not try to compare the results obtained from the reconstructed images. Of course, EIT is not only a modality to detect changes, but also to create images of conductivity distribution. Thus, in this study, the image frames of the models have also been reconstructed and then, the characteristics of the reconstructed conductivity change images have been evaluated, using some figures of merit.

Reconstructed images: Conductivity distribution of all frames of the elliptical forward models are reconstructed applying the "Maximum A Posteriori" regularized inverse and the forward measurement data. In this study, 9 frames have been considered for the models in which inhomogeneity moves along the major horizontal axis and 5 frames have also been considered for the models with the contrast moving along the minor vertical axis for each of the chosen current patterns. Thus, $13\times4 = 52$ frames have been totally considered in this study, considering that the central frame is repeated in both the horizontal and vertical movements of the contrast. In addition, for each frame of the defined models, conductivity change images have been reconstructed in three cases which have been discussed in section 1. Considering the three cases assumed for each frame, the total number of reconstructed images is $52\times3 = 156$ and therefore, it is not reasonable to show all the reconstructed images in this paper, due to space constraints.

Figure 2 shows the reconstructed conductivity change images of the 5th frame from the nine frames of elliptical model number 1 in that the inhomogeneity moves aligning the major horizontal axis of the ellipse from the left to the right side and the neighboring current-voltage pattern has been applied. Also, Fig. 3 shows the first

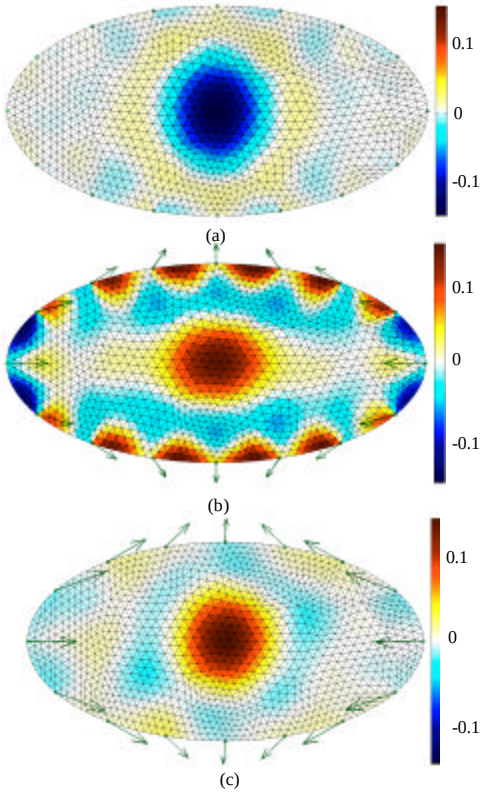

Fig. 2: The reconstructed conductivity change images of the 5th frame of elliptical model number 1 (central frame) in that the neighboring current-voltage pattern has been applied and the contrast moves aligning the major axis of the ellipse from a to c assuming the three cases (a) The boundary has no deformation, (b) The boundary has a 1% deformation and images have been reconstructed by applying the standard algorithm and (c) The boundary has a 1% deformation and images have been reconstructed by applying proposed algorithm. Green arrows indicate each electrode's displacement, scaled by 20

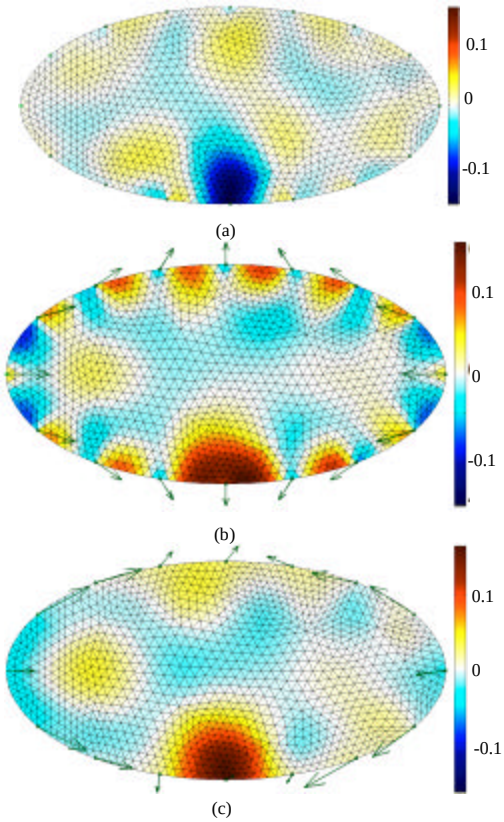

Fig. 3: The reconstructed conductivity change images of the first frame of elliptical model number 8 in that the trigonometric current-voltage pattern has been applied and the contrast moves aligning the minor axis of the ellipse from the bottom to the top side assuming three cases (a) The boundary has no deformation, (b) The boundary has a 1% deformation and images have been reconstructed by applying the standard algorithm and (c) The boundary has a 1% deformation and images have been reconstructed by applying proposed algorithm. Green arrows indicate each electrode's displacement, scaled by 20

frame from the five frames of elliptical model number 8 in that the contrast moves aligning the minor vertical axis of the ellipse from the bottom to the top side, and the trigonometric current-voltage pattern has been applied. The conductivity change images have been coloured with the blue-red spectrum shown to the right of the images. Green arrows indicate each electrode's displacement, scaled by 20. The characteristics of the reconstructed conductivity change image have been quantified using three figures of merit which are blur radius, artifact amplitude measure and position error, respectively.

Blur radius (BR): The blur radius measures the square root of the ratio of the area of the disk, centered on the inhomogeneity centre that encircles elements containing half the total image intensity to the total are of the reconstruction model. Blur radius is a measure of PSF area and is considered as the most well known criterion to estimate the spatial resolution of the reconstructed images in EIT (Wheeler *et al*., 2002). BR can be written as:

$$BR = \frac{r_z}{r_{tot}} = \sqrt{\frac{A_z}{A_{tot}}} \quad (24)$$

where, r_{tot} and A_{tot} are the radius and area of the FEM reconstruction model and r_z and A_z are the radius and area

Table 1: The blur radius values calculated from all reconstructed conductivity change image frames of models number 1-8, for cases 1-3

Models	Cases	[-0.8,0] [0,-0.4]	[-0.6,0]	[-0.4,0] [0,-0.2]	[-0.2,0]	[0,0] [0,0]	[+0.2,0]	[+0.4,0] [0,+0.2]	[+0.6,0]	[+0.8,0] [0,+0.4]	Average	Variance
1	1	0.196	0.188	0.212	0.218	0.226	0.220	0.210	0.194	0.192	0.206	0.000
	2	0.317	0.334	0.334	0.341	0.337	0.333	0.326	0.328	0.317	0.330	0.000
	3	0.204	0.209	0.220	0.238	0.240	0.230	0.218	0.206	0.202	0.219	0.000
2	1	0.164	0.000	0.210	0.000	0.226	0.000	0.218	0.000	0.162	0.196	0.001
	2	0.260	0.000	0.339	0.000	0.337	0.000	0.340	0.000	0.262	0.308	0.002
	3	0.160	0.000	0.226	0.000	0.240	0.000	0.227	0.000	0.165	0.204	0.001
3	1	0.209	0.199	0.220	0.250	0.307	0.263	0.226	0.219	0.190	0.232	0.001
	2	0.295	0.320	0.337	0.337	0.341	0.339	0.332	0.324	0.304	0.326	0.000
	3	0.207	0.222	0.268	0.317	0.317	0.295	0.267	0.228	0.217	0.260	0.002
4	1	0.192	0.000	0.240	0.000	0.307	0.000	0.252	0.000	0.195	0.237	0.002
	2	0.263	0.000	0.342	0.000	0.341	0.000	0.349	0.000	0.265	0.312	0.002
	3	0.190	0.000	0.280	0.000	0.317	0.000	0.324	0.000	0.196	0.261	0.004
5	1	0.231	0.263	0.329	0.302	0.294	0.270	0.250	0.212	0.211	0.262	0.002
	2	0.350	0.374	0.381	0.353	0.355	0.355	0.380	0.350	0.311	0.357	0.000
	3	0.339	0.366	0.378	0.323	0.344	0.353	0.369	0.319	0.309	0.344	0.001
6	1	0.188	0.000	0.254	0.000	0.294	0.000	0.304	0.000	0.229	0.254	0.002
	2	0.292	0.000	0.368	0.000	0.355	0.000	0.354	0.000	0.293	0.333	0.001
	3	0.267	0.000	0.369	0.000	0.344	0.000	0.333	0.000	0.259	0.314	0.002
7	1	0.185	0.217	0.248	0.255	0.263	0.263	0.248	0.219	0.189	0.232	0.001
	2	0.302	0.329	0.336	0.333	0.339	0.341	0.343	0.330	0.303	0.329	0.000
	3	0.238	0.254	0.259	0.285	0.300	0.317	0.279	0.252	0.229	0.268	0.001
8	1	0.203	0.000	0.246	0.000	0.263	0.000	0.252	0.000	0.221	0.237	0.001
	2	0.295	0.000	0.349	0.000	0.339	0.000	0.347	0.000	0.285	0.323	0.001
	3	0.260	0.000	0.310	0.000	0.300	0.000	0.323	0.000	0.225	0.284	0.002

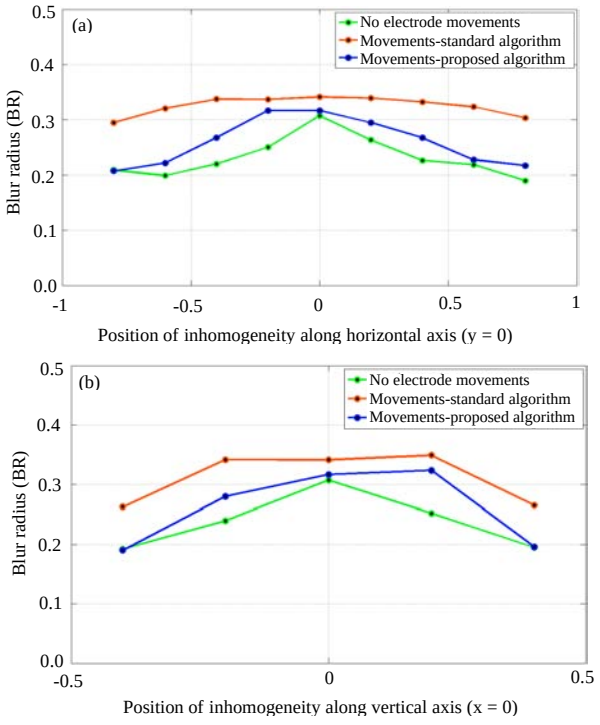

Fig. 4: The blur radius variations versus contrast positioning for the models with the opposite current pattern, (a) the major axis and (b) the minor axis

of the region including half the total intensity of all the elements in the reconstructed image, respectively.

Table 1 shows the blur radius values calculated from all reconstructed conductivity change images. This Table includes 8 subsets that correspond to 8 defined models. Each subset is constructed from three rows indicating the results obtained from the three cases introduced in section 1.In addition, this table has eleven columns. Columns 1 to 9 indicate the frames for each of the models frames for each row. Also, four blank spaces are observed in each row for the models in which five frames have been considered. and the introduced cases, while the other two demonstrate, respectively, the mean and variance of these Figure 4 also represents BR variations of the reconstructed images versus positioning of the inhomogeneity centre along the two main axes of the ellipse for the 3rd and 4th models in which the opposite current pattern has been applied. In this Fig. 4, the green curve corresponds to the first case, the red curve relates to the second case and the blue curve represents the third case introduced.

Blur radius values in case 1:

- According to Table 1, for case 1 in which the models have been assumed to have no deformation, the models with the neighboring current-voltage pattern have led to lower blur radius mean than the other ones. These values are, respectively, 0.2061 and 0.1959 for models number 1 and 2, while the models in which the cross current pattern has been applied have resulted in the poorest mean values that are 0.2625 and 0.2537 for the 5th and 6th models, respectively

- Comparing frames in each model shows that the blur radius values increase when the contrast moves from the boundary toward the central point of the ellipse along the radial axes. This is due to factors such as either the attenuation of current density by the medium resistivity, or the divergence of both the current flow and the isopotential lines with an increase in distance to the peripheral electrodes. This point is observable from the green curves in Fig. 4 where the graphs correspond to the models in which the opposite current pattern has been applied. It is mentionable that only for model number 5 in that the contrast moves along the horizontal axis and the cross current pattern has also been applied, the point of maximum blur radius value has shifted to the left side of the ellipse centre, because of the effects of constant reference electrodes that are discussed above
- The values obtained from the last column of Table 1 show that the models in which the cross or opposite current-voltage pattern has been applied lead to a higher blur radius variance between the frames of each model. The values are, respectively, 0.0017 and 0.0023 for models number 5 and 6, but are lower than 0.001 for the models in which the neighboring or the trigonometric current patterns have been applied. This shows that applying the cross or opposite current pattern causes more variations in the blur radius values when the introduced contrast moves across the area of the elliptical model
- Making a comparison between the central contrast frames in all models shows that the models with the neighboring current pattern are the best ones in terms of blur radius. This value is 0.226, which is the same in the first and second models because of repeating this special frame in both of the models. Additionally, the opposite and cross current patterns result in the poorest BR values for the central contrast, so these values are 0.3074 and 0.2936 for these models, respectively. Generally, it seems that because of the effects of deviation of the models from circular and isotropic geometry, as well as the divergence of the current flow and isopotential lines, the nonuniformity of these lines due to passing through the inhomogeneity in the central regions is much higher than the boundary regions
- The opposite and cross pattern are more sensitive to these effects than the neighboring and trigonometric patterns, because, for instance, in the opposite current stimulation, the current is fed through a pair of diametrically opposed electrodes and thus, the diameter length variations in the ellipse distort the current density distribution more than the other patterns. Additionally, for the opposite stimulation divergence of the current flow lines is more than the other current patterns in the central region. Thus, applying the opposite pattern, it is reasonable that an increase in the current flow divergence in the central regions with respect to patterns such as the neighboring or trigonometric, causes a greater distortion of the current flow lines due to passing through the contrast
- Similar comparison between the side contrast frames shows that the mentioned effects are approximately modified when the contrast moves from the centre to the boundary of the ellipse, because of a decrease in the discrepancy of divergence of the current flow lines between applying different current patterns
- The main consequence of this part of the study is to comment that we must not definitively predict that a higher distinguishability leads to a higher resolution in the reconstructed images. This is because distinguishability can be considered as a measure of current density distributions, while resolution in the reconstructed images is affected by factors such as the divergence and nonuniformity of the current flow and the isopotential lines as well as the current density

Blur radius values in case 2: In this case, a 1% boundary deformation has been applied to all the nodes of the models. This deformation is demonstrated in Fig. 2b and 3b by green vectors that are scaled by 20. The assumed deformation simulates, for instance, the expansion of the chest due to inhalation:

- As the deformation is introduced, the electrode displacements negatively influence blur radius values. Comparing the blur radius mean values between cases 1 and 2 in all models shows that these effects manifest, increasing in blur radius mean in the range of 31 to 60%
- These effects are more observable in the models in which the neighboring current pattern has been applied, so the assumed deformation causes a 59.9 and 57% increase in blur radius mean for the first and second models, respectively. This is because the neighboring current pattern leads to significant current density near the boundary and electrode displacement causes the current flow and isopotential lines to distort sharply, so that the changes in the sensitivity distribution field across the entire domain are more observable. But using the cross and opposite current patterns lead to the

minimum values in terms of blur radius mean sensitivity to electrode displacements. These results agree with the previous similar study for a circular homogenous model which reported that the opposite method is much less sensitive to electrode displacements than the neighboring. However, those studies are focused on current density distributions and did not attempt to reconstruct the conductivity images (Oh and Sadleir, 2005)

- The discrepancies between the current patterns have been modified for the side frames in this term. This is because, in the boundary regions, although either the current density or the divergence of the current flow and isopotential lines are much higher, they change slightly less than the central region for each point, applying different current patterns either the current density or the divergence of the current flow and isopotential lines are much higher, they change slightly less than the central region for each point, applying different current patterns
- Making a comparison between the frames in each model shows that the side contrast frames lead to much higher BR sensitivity to electrode displacements than in central contrast ones. This is exactly because of either a much higher current density or greater convergence of the current flow and isopotential lines in the boundary regions than in the centre
- The blur radius sensitivity to electrode movements slightly increases, when the contrast translates from the minor to the major axis aligned by an elliptical curved line with an equation of:

$$x^2 + 4y^2 = r^2 (r < 1)$$

applying the deformation assumed in this study.

Blur radius values in case 3: Comparing the proposed and standard algorithms, the proposed algorithm produces marginally lower blur radius. Assessing these results, the proposed algorithm blur radius mean values are 5.5-34% smaller than the standard algorithm for the 1% boundary deformation assumed in this work. The reduction of blur radius applying the proposed algorithm relative to the standard algorithm is defined as blur radius gain, which evaluates the performance of the proposed algorithm in terms of contrast blurring reduction.

$$G = \frac{BR_s - BR_p}{BR_s} \quad (25)$$

The best blur radius mean gain values have resulted for the models with the neighboring current pattern in the order of 34%, while the poorest values have been obtained for the cross current pattern in the order of 5%.

Also, the proposed algorithm had better performance for side contrast frames than central ones in terms of BR reduction from the centre toward the boundary of the ellipse.

Artifact amplitude measure (AAM): The reconstruction artifact is defined as the elements of non-zero conductivity variation, which is known a priori from the physical or simulation model (Gomez-Laberge, 2006). To measure these effects, a measure of reconstruction artifact amplitude is defined as follows. The artifact Amplitude Measure is defined by the expression:

$$AAM = \sqrt{\frac{\sum_{i \in L} S_i x_i^2}{\sum_{i \in L} S_i}} \quad (26)$$

where, $S_i \subset S$ is the area of element i, x_i is the intensity of element i and L is a subset of elements selected. In this study, L has been considered as elements that are out of the contrast region. Table 2 represents the artifact amplitude measure values calculated from all reconstructed conductivity change image frames. The structure of this table is exactly similar to Table 1.

Artifact amplitude measure values in case 1:

- According to Table 2, for the case in which the models have been assumed to have no deformation, the models with the trigonometric current patterns have led to a lower artifact amplitude measure mean values than the others. These values are 0.0257 and 0.0298 for the 7th and 8th models, respectively. This is because the current flow lines do not diverge, using the trigonometric patterns. Thus, the distortion of the current flow lines due to passing through the inhomogeneity broadens slightly less than the other patterns. But applying the cross pattern has caused the poorest results in this term, so the mean values are respectively 0.0379 and 0.0382 for the 5th and 6th models, respectively. In addition, the neighboring pattern has led to better AAM mean than the opposite one
- Comparing the frames in each model shows that AAM values increase when the contrast moves from the centre toward the boundary of the ellipse. This is because the divergence of the current flow and isopotential lines that are distorted due to passing through the contrast medium, broadens the location and magnifies the intensity of the artifacts. Thus, it is predictable that the artifacts increase for the

Table 2: The artifact amplitude measure values calculated from all reconstructed conductivity change image frames of models number 1-8, for cases 1-3

Models	Cases	[-0.8,0] [0,-0.4]	[-0.6,0]	[-0.4,0] [0,-0.2]	[-0.2,0]	[0,0]	[+0.2,0]	[+0.4,0] [0,+0.2]	[+0.6,0]	[+0.8,0] [0,+0.4]	Average	Variance
1	1	0.041	0.033	0.029	0.023	0.024	0.024	0.030	0.034	0.040	0.031	0.000
	2	0.065	0.061	0.060	0.058	0.058	0.059	0.060	0.061	0.064	0.061	0.000
	3	0.046	0.034	0.028	0.023	0.023	0.025	0.030	0.032	0.039	0.031	0.000
2	1	0.041	0.000	0.030	0.000	0.024	0.000	0.027	0.000	0.040	0.032	0.000
	2	0.064	0.000	0.059	0.000	0.058	0.000	0.056	0.000	0.064	0.060	0.000
	3	0.045	0.000	0.030	0.000	0.023	0.000	0.028	0.000	0.044	0.034	0.000
3	1	0.045	0.036	0.030	0.023	0.020	0.024	0.032	0.039	0.040	0.032	0.000
	2	0.072	0.068	0.068	0.064	0.065	0.065	0.071	0.070	0.072	0.068	0.000
	3	0.049	0.038	0.034	0.030	0.031	0.032	0.040	0.039	0.043	0.037	0.000
4	1	0.047	0.000	0.033	0.000	0.020	0.000	0.029	0.000	0.048	0.036	0.000
	2	0.073	0.000	0.067	0.000	0.065	0.000	0.065	0.000	0.073	0.069	0.000
	3	0.054	0.000	0.037	0.000	0.031	0.000	0.034	0.000	0.053	0.042	0.000
5	1	0.051	0.046	0.041	0.031	0.031	0.027	0.035	0.037	0.041	0.038	0.000
	2	0.100	0.087	0.093	0.084	0.075	0.090	0.083	0.080	0.069	0.084	0.000
	3	0.082	0.071	0.076	0.060	0.047	0.071	0.056	0.062	0.052	0.064	0.000
6	1	0.042	0.000	0.037	0.000	0.031	0.000	0.034	0.000	0.046	0.038	0.000
	2	0.094	0.000	0.082	0.000	0.075	0.000	0.084	0.000	0.083	0.083	0.000
	3	0.080	0.000	0.066	0.000	0.047	0.000	0.063	0.000	0.064	0.064	0.000
7	1	0.033	0.027	0.024	0.020	0.021	0.022	0.026	0.027	0.031	0.026	0.000
	2	0.061	0.058	0.057	0.057	0.055	0.054	0.055	0.058	0.059	0.057	0.000
	3	0.040	0.029	0.029	0.024	0.023	0.022	0.026	0.029	0.038	0.029	0.000
8	1	0.039	0.000	0.025	0.000	0.021	0.000	0.022	0.000	0.042	0.030	0.000
	2	0.061	0.000	0.057	0.000	0.055	0.000	0.055	0.000	0.064	0.058	0.000
	3	0.040	0.000	0.026	0.000	0.023	0.000	0.024	0.000	0.045	0.032	0.000

contrasts which are closer to the electrodes, because of much higher magnification of AAM intensity in the entire medium due to divergence of the current flow and isopotential lines from the boundary to the centre of the model

- The comparison between the models also illustrates that the opposite current pattern has caused a higher artifact amplitude variance for the frames of each models with values of 7.43e-5 and 1.41e-4 for the 3rd and 4th models, respectively. This is due to steeper changes in the divergence of current flow lines across the entire medium, applying this current pattern. Figure 5 demonstrates the AAM variations of the reconstructed images versus positioning of the inhomogeneity centre along the two main axes of the ellipse for the 3rd and 4th models in that the opposite current pattern has been applied
- Central frames in all the models show that the opposite and trigonometric current patterns have led to better values, while the cross pattern has caused the poorest results in this term. A much higher decrease in AAM values for the central frame relative to side one for the models with opposite current patterns is due to a much steeper convergence of the current flow lines from the centre to the boundary of the ellipse. Thus, applying the opposite current pattern, the negative influence of distortion of the current flow and isopotential lines due to central inhomogeneity becomes less than in the other patterns
- The same comparison between the side contrasts shows that the trigonometric current pattern has led to the best results, while the cross pattern has caused the poorest. Furthermore, the results obtained from the opposite pattern are poorer than the neighboring one for the side frames because of a much steeper divergence of current flow lines from the boundary to the centre of the ellipse, applying the opposite current pattern
- Generally, we comment that the distribution of the artifact in the reconstructed images explicitly depends on the procedure of divergence of the current flow and isopotential lines across the entire image

Artifact amplitude measure values in case 2:

- According to Table 2, the boundary deformation has deteriorated the reconstructed images in terms of AAM. Comparing the AAM mean values between cases 1 and 2 in all models illustrates that these effects manifest increase in these values more than twice as high. The largest increase in AAM mean values can be observed for the models with the cross current pattern, whereas applying the neighboring current pattern has led to the lowest increase, so the increases for the first and second models are 1.96 and 1.85, respectively
- Comparing the side contrast frames instead of the mean values of frames leads to the same ranking between the applied current patterns. In addition, considering the side frames of model number 5 shows that AAM sensitivity to electrode displacements for the side contrasts that are closer to the reference

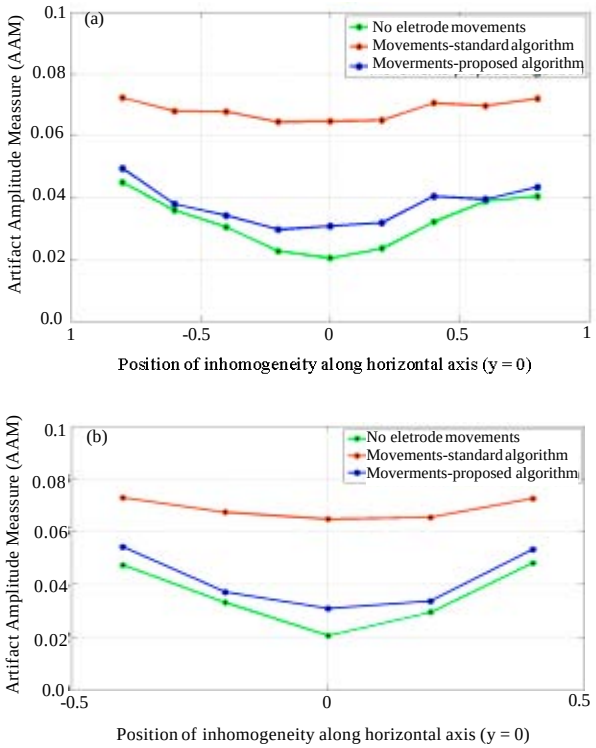

Fig. 5: The artifact amplitude measure variations versus contrast positioning for the models with the opposite current pattern, (a) The major axis and (b) The minor axis

current and voltage electrodes are much higher than the other frames because of the effects of the reference electrodes and the procedure of divergence of the corresponding flow lines which have been discussed above

- Considering central frames also shows that the opposite current pattern has led to a more sensitivity to electrode displacements than the others, while the neighboring pattern has resulted in a less sensitivity to these effects
- Comparing the frames in each model shows that the central contrast frames have led to greater artifact amplitude increase than those of the side contrast due to boundary deformation. This is because artifacts due to boundary deformation usually occur in the regions with a higher current density distribution, for instance near the boundary, not necessarily around the contrast. Thus, when the contrast moves toward the boundary regions which have a higher current density, some of these artifacts are excluded due to their inclusion in the contrast regions. In other words, the location of occurring artifacts due to electrode displacements is less dependent on contrast positioning than broadening artifact. Thus, the movement of the contrast toward the boundary would cause a decrease in augmented AAM values via excluding the artifactual elements which are encircled by the contrast, and so are not taken into account in the AAM calculation
- Similar to BR values, the AAM sensitivity to electrode movements has slightly increased when the contrast translates from the minor to the major axis aligned by an elliptical curved line with an equation of $x^2+4y^2 = r^2$ ($r<1$), due to the effects of the boundary anisotropy

Artifact amplitude measure values in case 3: Comparing the proposed and standard algorithms, the proposed algorithm is more tolerant to electrode displacements and maintains a much lower AAM. Evaluating the results shows that the proposed algorithm AAM mean values are 24-50% smaller than the standard algorithm for the 1% boundary deformation assumed in this study. The decrease in the AAM values obtained from the proposed algorithm relative to those of the standard algorithm is defined as AAM gain, which estimates the performance of the proposed algorithm in terms of artifact reduction:

$$G_{AAM} = \frac{AAM_s - AAM_p}{AAM_s} \quad (27)$$

Applying the proposed algorithm, the trigonometric and neighboring current patterns have led to greater AAM mean gain than the other patterns. These mean gain values are 49.54 and 45.52% for the 7th and 8th models, or 48.58 and 43.53% for the first and second ones, respectively. However, the proposed algorithm had a poorer performance for the models with the cross current pattern, so the AAM gain values are 24.11 and 23.27% for the 5th and 6th models, respectively. In addition, a fair comparison between the central or side frames instead of the mean of the frame values leads to similar ranking. Additionally, comparing the frames of each model illustrates that the proposed algorithm had better performance for the central contrast frames than the side ones in terms of the AAM reduction. Additionally, the AAM reduction improves when the contrast translates from the minor to the major axis aligning the elliptical curved lines introduced above.

Position error (PE): The position error measures the discrepancy of the contrast centre between the forward FEM model and reconstructed images. It can be defined

Table 3: The blur radius values calculated from all reconstructed conductivity change image frames of models number 1-8, for cases 1-3

Models	Cases	[-0.8,0] [0,-0.4]	[-0.6,0]	[-0.4,0] [0,-0.2]	[-0.2,0]	[0,0] [0,0]	[+0.2,0]	[+0.4,0] [0,+0.2]	[+0.6,0]	[+0.8,0] [0,+0.4]	Average	Variance
1	1	0.044	0.021	0.005	0.003	0.006	0.006	0.010	0.009	0.063	0.019	0.000
	2	0.419	0.355	0.238	0.141	0.016	0.101	0.195	0.319	0.408	0.244	0.020
	3	0.049	0.023	0.012	0.004	0.011	0.011	0.005	0.011	0.059	0.021	0.000
2	1	0.007	0.000	0.022	0.000	0.006	0.000	0.029	0.000	0.016	0.016	0.000
	2	0.124	0.000	0.165	0.000	0.016	0.000	0.156	0.000	0.114	0.115	0.004
	3	0.026	0.000	0.026	0.000	0.011	0.000	0.030	0.000	0.022	0.023	0.000
3	1	0.034	0.022	0.006	0.010	0.040	0.023	0.009	0.018	0.036	0.022	0.000
	2	0.470	0.355	0.257	0.131	0.028	0.139	0.205	0.361	0.380	0.258	0.021
	3	0.059	0.026	0.016	0.100	0.100	0.033	0.015	0.016	0.039	0.045	0.001
4	1	0.012	0.000	0.030	0.000	0.040	0.000	0.015	0.000	0.025	0.024	0.000
	2	0.120	0.000	0.182	0.000	0.028	0.000	0.166	0.000	0.165	0.132	0.004
	3	0.015	0.000	0.036	0.000	0.100	0.000	0.068	0.000	0.012	0.046	0.001
5	1	0.025	0.024	0.167	0.005	0.040	0.006	0.012	0.017	0.055	0.039	0.003
	2	0.470	0.499	0.448	0.272	0.098	0.255	0.283	0.374	0.430	0.348	0.017
	3	0.419	0.467	0.480	0.397	0.216	0.209	0.311	0.356	0.231	0.343	0.011
6	1	0.016	0.000	0.035	0.000	0.040	0.000	0.111	0.000	0.028	0.046	0.001
	2	0.221	0.000	0.158	0.000	0.098	0.000	0.264	0.000	0.258	0.200	0.005
	3	0.195	0.000	0.160	0.000	0.216	0.000	0.358	0.000	0.210	0.228	0.006
7	1	0.013	0.012	0.007	0.006	0.008	0.015	0.017	0.016	0.008	0.011	0.000
	2	0.446	0.372	0.277	0.147	0.014	0.194	0.292	0.383	0.473	0.289	0.022
	3	0.056	0.008	0.010	0.050	0.034	0.073	0.015	0.011	0.068	0.036	0.001
8	1	0.019	0.000	0.002	0.000	0.008	0.000	0.013	0.000	0.035	0.015	0.000
	2	0.219	0.000	0.163	0.000	0.014	0.000	0.143	0.000	0.203	0.148	0.007
	3	0.032	0.000	0.019	0.000	0.034	0.000	0.062	0.000	0.020	0.033	0.000

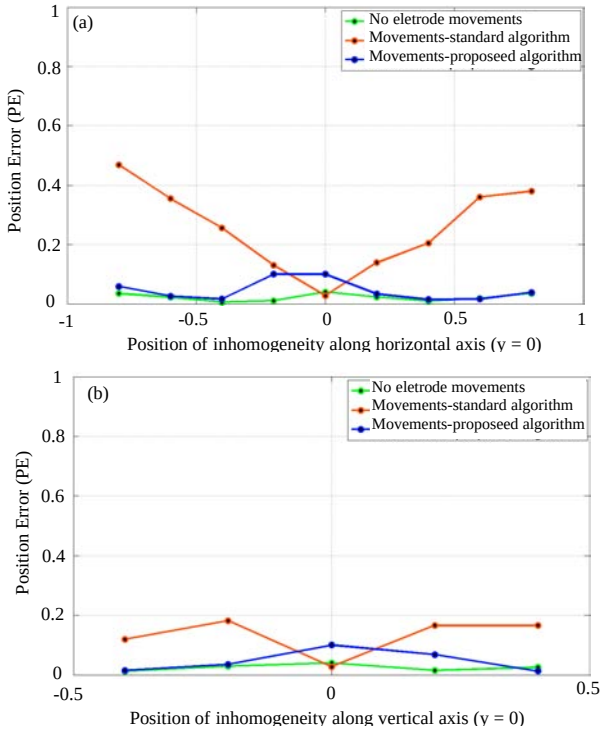

Fig. 6: The position error variations versus contrast positioning for the models with the opposite current pattern, (a) The major axis and (b) The minor axis

as a geometrical vector which evaluates both the magnitude and the angle of shifting the geometry of conductivity change images by the applied reconstruction algorithm (Adler *et al*., 2009). Table 3 represents the position error values calculated from all reconstructed conductivity change image frames. According to Table 3, for the case in which the models have been assumed to have no deformation, the PE values are in the order of 0.005-0.06. Also, the models in which the cross current pattern has been applied, have led to the greatest PE mean values, whereas the models with neighboring and trigonometric current patterns have led to the smallest. In addition, no meaningful changes between the frames of each model could be found for this case.

But the 1% deformation introduced in the forward model causes considerable position errors in the reconstructed images of all models. Assessing the direction of the PE vectors which are not introduced in Table 3 shows that this deformation has led to shifting the contrast to the centre of the ellipse. The magnitude of this shift has often been in the range of half the distance between the contrast centre and the ellipse centre.

This means that position error usually increases, when the contrast moves from the centre to the boundary of the ellipse. Hence, the PE sensitivity to electrode movements has been trivial for the central contrast frames. The source of these errors is the significant artifacts due to electrode displacements that are distributed near the peripheral electrodes and produce false images in the boundary regions. Because these false image regions are located symmetrically around the centre of the ellipse, their effects on PE are not considerable for the central contrast frames. However, these effects manifest much higher PE values for the contrasts which are located in the regions far from the ellipse centre.

In addition, the proposed algorithm was successful to compensate these errors, especially for the side contrast frames. Figure 6 shows the PE values for the models in which the opposite current pattern has been applied, assuming the three cases introduced in section 1.

DISCUSSION

This study deals with the effects of applying different common current-voltage patterns on reconstructed images of an elliptical model in which a contrast moves aligning the main axes of the ellipse. One limitation of former clinical work is that the body was assumed to be isotropic. Although, this is a reasonable approximation for the lung, it is far from true for applications such as detection and characterization of tumors, monitoring cancer ablation procedures, brain function imaging or even noninvasive imaging of heart function and blood flow. In this study, the 2D model has been chosen so that the effects of reconstruction model deviation from the previously used circular form on the reconstructed images can be investigated. The results can be useful for evaluating the anisotropy or ellipticity effects of organs being imaged on image reconstruction. The effect of parts of the domain being anisotropic is an interesting topic for further work.

First, we characterized the ability of the different applied current patterns to distinguish a small change in the internal conductivity distribution and analyzed it as a function of the contrast positioning. The results show that this measure depends on current density distribution across the medium and decreases symmetrically from the boundary to the centre of the ellipse. Only by applying the cross pattern, have the distinguishability values sharply increased for the points which are closer to the reference electrodes.

However, EIT is not only a technology for distinguishing changes, but also for obtaining images of conductivity distribution. The results obtained from the reconstructed images show that the blur radius increases for the central contrast frames with respect to the side frames in all models, for the case in which no deformation has been considered. This is because in the central regions, the current density uniformity is less than the boundary regions because of factors such as the attenuation of the current density distribution by the medium resistance or the divergence of the current flow lines due to greater distance to the peripheral electrodes. Additionally, the anisotropical geometry of the elliptical model causes a greater distortion of current density distribution in the central regions. The divergence of the isopotential lines increases in the central regions as well, and so, such nonuniformities lead to a higher distortions in the reconstructed images in these regions.

In addition, the AAM values have decreased when the contrast moves from the boundary to the centre of the ellipse, for the case in which no deformation has been considered. This broadening artifact is due to distortion of the current flow and isopotential lines via passing through the conductive inhomogeneity. The divergence of these lines broadens and magnifies the artifacts in the entire medium. Therefore, it is reasonable that the artifacts become much greater and broader for the inhomogeneities that are closer to the peripheral electrodes.

The boundary deformation occurs mostly in clinical EIT due to breathing or posture changes. The latter causes a displacement of the skin and so, the electrodes during measurements. The results show that boundary deformation negatively influences the reconstructed conductivity distributions. These effects manifest deterioration of contrast and also produce false conductive artifacts which are more observable in the vicinity of the displaced electrodes. Evaluating the results illustrates that blur radius and positioning error sensitivity to boundary deformation increases when the contrast is located in the regions in which a higher current density distribution exists. Furthermore, the artifacts due to electrode displacements have often occurred in the regions with higher current density, especially near the displaced electrodes. Thus, entering the contrast to these regions reduces these augmented artifacts because of including some of the artifactual elements in the contrast region. Therefore, AAM sensitivity to boundary deformation decreases when the contrast moves from the centre to the boundary of the ellipse.

In addition, several groups have proposed various algorithms in order to reduce and eliminate the errors due to boundary deformations in EIT. The most well known alternative is an algorithm proposed by (Soleimani *et al*., 2006) in order to reconstruct both conductivity changes and electrode displacements. In this study, their algorithm has been implemented and its performance compared between the different defined models, so that the algorithm performance has been investigated for different current patterns as well as various contrast positioning in terms of blur radius, artifact amplitude and position error reduction.

It is hoped that the simulated results in this study can be useful for improving image quality in clinical cases via using a prior knowledge about contrast positioning across the organs being imaged. This prior knowledge can be obtained using either anatomical structure mapping or the other imaging modalities such as MRI, CT, etc. Combination of EIT with the other imaging modalities has

been mostly considered in recent years. The authors anticipate that prior information about contrast positioning in an anisotropic domain can help researchers to apply the optimal current-voltage pattern based on this information in future clinical applications.

REFERENCES

Abbasi, A., B.V. Vahdat and G.E. Fakhim, 2009. An inverse solution for 2D electrical impedance tomography based on electrical properties of material blocks. J. Applied Sci., 10: 1962-1967.

Adler A. and W.R.B. Lionheart, 2006. Uses and abuses of EIDORS: An extensible software base for EIT. Physiol. Meas., 27: S25-S42.

Adler, A., J.H. Arnold, R. Bayford, A. Borsic and B. Brown *et al.*, 2009. A unified approach to 2D linear EIT reconstruction of lung images. Physio. Meas., 30: S35-S55.

Adler, A. and W.R. Lionheart, 2011. Minimizing EIT image artefacts from mesh variability in finite element models. Physiol. Meas., 32: 823-834.

Adler, A., P.O. Gaggero and Y. Maimiaitijiang, 2011. Adjacent stimulation and measurement patterns considered harmful. Physiol. Meas. 10.1088/0967-3334/32/7/S01.

Binjadhnan, F.A.M. and T. Ahmad, 2010. Semigroup of EEG signals during epileptic seizure. J. Applied Sci., 10: 1466-1470.

Elwakkad, A., N.E. Hassan, H. Sibaii, S. El-Zayat, L. Sherif, E.R. Hameed and A.A. Shaheed, 2011. Relationship between obesity and 8-hydroxy-2-deoxy guanosine as an oxidative marker in obese adolescents of giza. J. Med. Sci., 11: 231-235.

Ghorbel, M., M. Samet, A.B. Hamida and J. Tomas, 2006. A 16-electrode fully integrated and versatile CMOS microstimulator dedicated to cochlear implant. J. Applied Sci., 6: 2978-2990.

Gomez-Laberge, C., 2006.. Electrical impedance tomography for deformable media. M.Sc. Thesis, University of Ottawa, Canada.

Graham, B.M. and A. Adler, 2006. Objective selection of the hyperparameter for EIT. Physiol. Measur., 27: S65-S79.

Griffiths, H., 2001. Magnetic induction tomography. Meas. Sci. Tech., 12: 1126-1131.

Hassan, N.E., S.A. El-Masry, N.L. Soliman and M.M. EL-Batran, 2008. Different techniques for body composition assessment. J. Med. Sci., 8: 15-21.

Holder, D., 2004. Electrical Impedance Tomography: Methods, History and Applications. Institute of Physics Pub., London, ISBN: 9780750309523 Pages: 456.

IEC., 2005. Medical electrical equipment general requirements for basic safety and essential performance Brussels. International Electrotechnical Commission.

Jing-Lei, G. and W. Zhi-Jian, 2011. Parameter identifications of elliptic differential equation by hybrid particle swarm optimization. Inform. Technol. J., 10: 152-157.

Keto, T., L. Tianyou and E. Bakambo, 2006. Seismic modeling of the velocity components at the sea floor in frequency domain. J. Applied Sci., 6: 171-176.

Kolehmainen, V., M. Lassas and P. Ola, 2006. Inverse conductivity problem with an imperfectly known boundary. SIAM J. Applied Math., 66: 365-383.

Kumar, P., S.P. Singh, R. Manohar and J.P. Shukla, 2006. Moisture dependent electrical parameter as an indicator of germination of seed: A case study of poppy seed. Int. J. Agric. Res., 1: 534-544.

Lohcham, N.S., Y.C. Chen and H.J. Engels, 2002. Transthoracic bioimpedance measurement of cardiac responses to maximal cycle exercise in healthy adult females. Pak. J. Biol. Sci., 5: 104-106.

Loke, M.H. and T. Dahlin, 2002. A comparison of the Gauss-Newton and quasi-Newton methods in resistivity imaging inversion. J. Appl. Geophys., 49: 149-162.

Mirhosseini, N.Z., S. Shahar, N.A.M. Yusoff, M.M. Ghayour-Mobarhan, A.R. Derakhshan and M.T. Shakery, 2011. Lower level of physical activity predisposes Iranian adolescent girls to obesity and its metabolic consequences. Pak. J. Nutr., 10: 728-734.

Noor, J.A.E., 2007. Electrical impedance tomography at low frequencies. Ph.D Thesis, University of New South Wales.

Oh, S. and R. Sadleir, 2005. Sensitivity distribution field of electrical impedance tomography. COMSOL Multiphysics User's Conference, Boston, USA.

Polydorides, N. and H. McCann, 2002. Electrode configurations for improved spatial resolution in electrical impedance tomography. Measur. Sci. Technol., 13: 1862-1870.

Polydorides, N. and W.R.B. Lionheart, 2002. A MATLAB based toolkit for three-dimensional electrical impedance tomography: A contribution to the EIDORS project. Meas. Sci. Thechnol., 13: 1871-1883.

Saulnier, G.J., R.S. Blue, J.C. Newell, D. Isaacson and P.M. Edic, 2001. Electrical impedance tomography. IEEE Signal Process., 18: 31-43.

Soleimani, M., C. Gomez-Laberge and A. Adler, 2006. Imaging of conductivity changes and electrode movement in EIT. Physiol. Meas., 27: S103-S113.

Vauhkonen, M., 1997. Electrical impedance tomography and prior information. Ph.D Thesis, University of Kuopio, Finland.

Vauhkonen, M., D. Vadasz, P.A. Karjalainen, E. Somersalo and J.P. Kaipio, 1998.. Tikhonov regularization and prior information in electrical impedance tomography. IEEE Trans. Med. Imag., 17: 285-293.

Wheeler, J.L., W. Wang and M. Tang, 2002. A comparison of methods for measurement of spatial resolution in two-dimensional circular EIT images. Physiol. Meas., 23: 169-176.

Zhang, J. and R.P. Patterson, 2005. EIT images of ventilation: What contributes to the resistivity changes? Physiol. Meas., 26: S81-S92.